MDPI

Article

Potential Controlling Factors and Landslide Susceptibility Features of the 2022 Ms 6.8 Luding Earthquake

Siyuan Ma [1,2], Xiaoyi Shao [3,4] and Chong Xu [3,4,*]

1   Institute of Geology, China Earthquake Administration, Beijing 100029, China; masiyuan@ies.ac.cn
2   Key Laboratory of Seismic and Volcanic Hazards, Institute of Geology, China Earthquake Administration, Beijing 100029, China
3   National Institute of Natural Hazards, Ministry of Emergency Management of China, Beijing 100085, China; xiaoyishao@ninhm.ac.cn
4   Key Laboratory of Compound and Chained Natural Hazards Dynamics, Ministry of Emergency Management of China, Beijing 100085, China
*   Correspondence: xc11111111@126.com or chongxu@ninhm.ac.cn

Abstract: On 5 September 2022, a Ms 6.8 earthquake struck Luding County, Ganzi Tibetan Autonomous Prefecture, Sichuan Province, China. This seismic event triggered over 16,000 landslides and caused serious casualties and infrastructure damages. The aim of this study is to perform the detailed landslides susceptibility mapping associated with this event based on an updated landslide inventory and logistic regression (LR) modeling. Firstly, we quantitatively assessed the importance of different controlling factors using the Jackknife and single-variable methods for modeling landslide occurrence. Subsequently, four landslide susceptibility assessment models were developed based on the LR model, and we evaluated the accuracy of the landslide susceptibility mappings using Receiver Operating Characteristic (ROC) curves and statistical measures. The results show that ground motion has the greatest influence on landslides in the entire study area, followed by elevation, while distance to rivers and topographic relief have little influence on the distribution of landslides. Compared to the NEE plate, PGA has a greater impact on landslides in the SWW plate. Moreover, the AUC value of the SWW plate significantly decreases for lithological types and aspect, indicating a more pronounced lithological control over landslides in the SWW plate. We attribute this phenomenon primarily to the occurrence of numerous landslides in Permian basalt and tuff in the SWW plate. Otherwise, the susceptibility results based on four models indicate that high-susceptibility areas predicted by different models are distributed along both sides of seismogenic faults and the Dadu Rivers. Landslide data have a significant impact on the model prediction results, and the model prediction accuracy based on the landslide data of the SWW plate is higher.

Keywords: 2022 Luding earthquake; coseismic landslides; landslide susceptibility mapping; controlling factors; logistic regression (LR) model

1. Introduction

A Ms 6.8 earthquake struck Luding County in Sichuan Province, China, on 5 September 2022 at 12:52 local time. The epicenter was situated within the Hailuogou Glacier Forest Park in Moxi Town (29.59°N, 102.08°E) at a focal depth of roughly 16 km. The earthquake had a maximum intensity of IX at the China Earthquake Networks Center (www.ceic.ac.cn, accessed on 3 April 2024). As of 13 September, the earthquake resulted in the loss of 93 lives, with 25 individuals reported as missing. About 20% of the casualties were directly linked to collapsed buildings, while landslides accounted for over 80% of the fatalities and missing persons [1]. Furthermore, due to the complex terrain and fragile geological environment in the Luding zone, it is highly prone to landslides under seismic activity. Therefore, conducting earthquake-induced landslides susceptibility mapping is crucial for

enhancing the resilience of major engineering projects and safeguarding public safety in this area [2].

Currently, the main methods of the landslide susceptibility assessment induced by a single earthquake event include the physically based Newmark method, statistically based method, and data-driven method [3–5]. On a large-scale area, the physically based method requires extensive detailed data to provide reliable landslide susceptibility results. Consequently, when there is a lack of reliable and detailed parameters such as geotechnical parameters and ground motion data, the physically based model may not offer ideal prediction accuracy for large-scale seismic landslide susceptibility mapping [6–8]. The statistical model simplifies the relationships among variables in the data through mathematical equations, but it has certain limitations in revealing the complex nonlinear interactions among environmental factors in susceptibility modeling [9–11]. The data-driven model learns from data without relying on predefined functions and extensive prior knowledge, thus achieving high evaluation accuracy [12,13]. As a result, data-driven models have been widely applied in landslide susceptibility assessments, including support vector machines (SVMs) [14], the LR model [15], random forest (RF) [12], and convolutional neural networks (CNNs) [16].

For the Luding earthquake, relevant studies about the coseismic landslides of the Luding earthquake mainly focused on landslide automatic identification [17,18], the establishment of landslide inventory [1,19–22], spatial distribution characteristics of landslides [2,23], and the rapid assessment of landslide susceptibility [1,22,24,25]. Relevant studies have conducted rapid susceptibility assessments of seismic landslides associated with this event using the physical–mechanical Newmark method [24,25] and data-driven method [18,22]. These results have effectively guided the deployment of rescue personnel and the allocation of resources for the Luding earthquake. For example, Liu et al. [25] conducted a rapid susceptibility assessment of earthquake-induced landslides using the Newmark method. The results showed that the area of potential high susceptibility is approximately 45 km^2, primarily distributed on both sides of the Dadu Rivers and west of the Xianshuih Fault. Djukem et al. [24] conducted a comparison between a traditional and an improved Newmark method for coseismic landslide prediction. The results show that the traditional equation is better suited for earthquakes similar to that of the Luding earthquake, with a higher concentration of landslides in the epicentral region. Wang et al. [18] obtained the landslide susceptibility result of the Luding earthquake within 2 h after the event using a near-real-time predictive model of coseismic landslides, which is built based on the global coseismic landslide database and deep learning algorithms. Chen et al. [22] employed multi-temporal optical satellite imagery interpretation and InSAR technology to interpret pre-earthquake landslides in the Luding area and combined the SVM method with 12 potential controlling factors to map the susceptibility of landslides induced by the Luding earthquake.

However, it should be noted that the accuracy of the susceptibility mapping for the Luding event in the above-mentioned study is limited. For the Newmark method, due to limitations inherent in the input parameters, the susceptibility results obtained by the Newmark method often exhibit significant disparities when compared to actual landslide distributions [24,26]. For the data-driven model, landslide data are the most critical factor affecting the accuracy of landslide susceptibility modeling. However, no relevant landslide susceptibility mapping of this event has been studied in detail based on the existing landslide inventory, and the existing landslide inventory often has serious omissions in landslide interpretations due to cloud cover on the west side of the seismogenic fault [20,27]. Consequently, the predictive models based on these landslide inventories often yield significantly underestimated predictive results for the west side of the seismogenic fault. Furthermore, an existing susceptibility assessment overlooked the differences in the potential controlling factors of both sides of the seismogenic fault [27]. This phenomenon resulted in landslide susceptibility mapping being unable to reflect the potential landslide

hazard zoning, thereby impacting the subsequent disaster prevention and mitigation in the study area.

Therefore, the aim of this study is to construct a detailed and objective landslides probability assessment map of the Luding earthquake based on an updated landslide inventory. We quantitatively assessed the importance of eight causative factors using Jackknife and univariate methods for modeling landslide occurrence. Subsequently, four landslide susceptibility assessment models were developed based on the LR model, and the accuracy of the landslide mappings was evaluated using the ROC curve and statistical indices. Finally, we quantitatively evaluated the landslide susceptibility maps of four models. This study can provide a reference for post-earthquake reconstruction planning, the analysis of long-term disaster effects after the earthquake events. Meanwhile, the predictive model can offer technical support for seismic landslide susceptibility assessments in the Sichuan–Yunnan region.

2. Tectonic and Geological Setting of the Luding Area

The Xianshuihe Fault is one of the most active fault zones in mainland China, with a total length of approximately 400 km [28]. In the past 300 years, this fault zone has experienced 25 earthquakes with magnitudes of M ≥ 6.0 and 8 earthquakes with magnitudes of M ≥ 7.0. The Luding earthquake is a destructive earthquake that occurred on the Xianshuihe Fault after the Ms 7.6 Lu-Huo earthquake in 1973 and the Ms 6.9 Dao-Fu earthquake in 1981 (Figure 1). The GPS and InSAR data reveal that the seismogenic fault of this event is the Moxi segment of the Xianshuihe Fault, with predominantly left-lateral strike-slip motion [29,30].
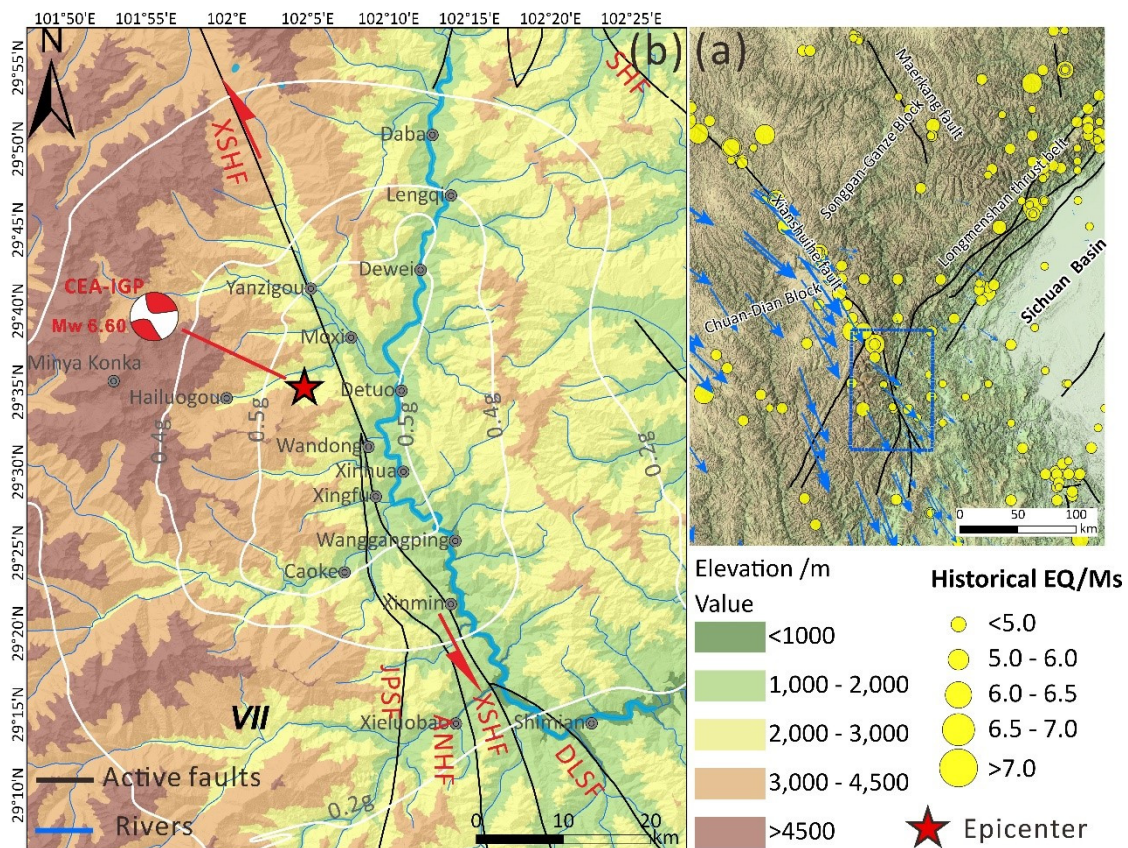

Figure 1. The tectonic setting and topographic feature of the Xianshuihe Fault and adjacent areas. (**a**) The distribution of the GPS velocity and historical earthquakes of the Xianshuihe Fault and adjacent areas. (**b**) The distribution of the elevation, active faults, and peak ground motion (PGA) of the Luding earthquake.

The quake-affected area is situated in the Hengduan Mountains on the southeastern edge of the Qinghai–Tibet Plateau, representing a typical high-mountain canyon region. The highest peak, Mount Gongga, reaches an elevation of 7556 m, with a horizontal distance of only about 30 km from the Dadu Rivers Valley in Dongpo and a relative height difference of over 6000 m (Figure 1). Due to the special geological and geomorphological conditions, the study area affected by the 2008 Ms 8.0 Wenchuan earthquake and the 2013 Ms 7.0 Lushan earthquake has led to the fragmentation and reduced stability of rock masses, which makes it more susceptible to geological hazards. The climate in the Luding area is influenced by the high-mountain terrain and the climate of the Qinghai–Tibet Plateau, with significant seasonal changes and obvious characteristics of the plateau monsoon climate. The Luding area experiences an average annual temperature of 15.5 °C and an average annual rainfall of 664.4 mm.

The lithology distribution shows that Plagioclase granite and diorite granite (G) and a Diorite vein (*Dio*) dominate the eastern portion of the seismogenic fault, covering the largest area. In the western region, Permian basalt (P_{2b}) forms the second-largest geological composition. Triassic limestone and Triassic and Devonian quartz sandstone ($T_L\&D_s$) are prevalent in the northeastern area. Quaternary sediments (Q_l) are primarily distributed along both sides of the Dadu Rivers and their tributaries. Additionally, the study area features Lower Permian tuff and breccia (P1t), Jurassic and Devonian mudstone, Ordovician and Silurian limestone and shale ($J_m\&O_{ls}$), and Sinian rhyolite (S_{rh}) (Figure 2).
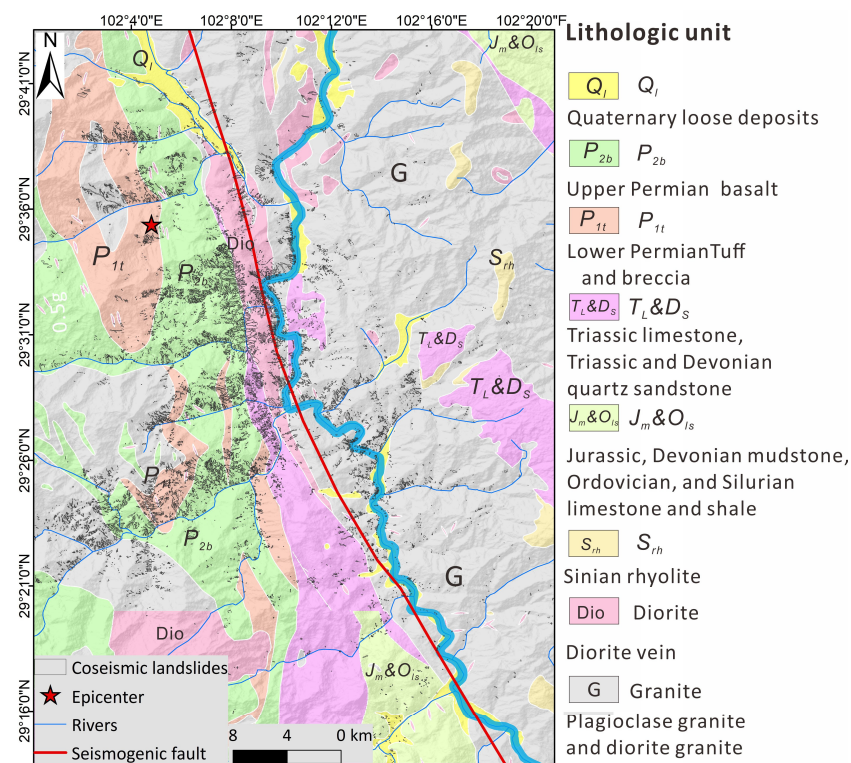

Figure 2. The lithological distribution of the Luding area. The 1:200,000 geological map is downloaded from the China Geological Survey Bureau (http://dcc.cgs.gov.cn/, accessed on 4 February 2024).

3. Materials and Methods

3.1. The 2022 Luding Landslide Inventory

High-resolution satellite images taken before and after the earthquake allow for a visual interpretation of coseismic landslides. Extensive landslide mapping was conducted using 3-m resolution optical Planet satellite images. The pre-earthquake images were captured between 1 June and 5 September 2022, while the post-earthquake images were taken from 8 September to 30 December 2022 [27]. In addition, we used pre- and post-earthquake satellite images from the Google Earth platform as supplementary image data.

The pre-earthquake satellite images are dated 22 December 2021, and the post-earthquake images are dated 10 September 2022. To ensure the accuracy and comprehensiveness of our landslide interpretation and to avoid misidentifying pre-earthquake landslides as coseismic events, we checked several identified landslide sites by field investigation [2]. Figure 3 shows the coseismic landslides based on pre-quake (Figure 3a) and post-quake (Figure 3b) Google Earth images located in the Wangdong area. Based on satellite images and field investigations, it is evident that the Wangdong Village area experienced the most intensive landsliding area during the earthquake. There are many landslides developed in this area, and the scale of landslides is relatively large. Figure 4 shows the pre- and post-quake images located near the Wanggangping area, where a large number of small-scale landslides have developed, mainly consisting of soil collapses, shallow landslides, and rolling stones [2]. Compared to the Wangdong area, although the Wanggangping region has developed a large number of landslides, the scale of the landslides is relatively small, and few medium- and large-sized landslides have developed.

Figure 3. Map showing the coseismic landslides based on pre- and post-quake Google Earth images located in the Wangdong area. (**a**) Pre-quake satellite image. (**b**) Post-quake satellite image.

According to the latest landslide database [27], the Luding earthquake triggered about 16,033 landslides, with a total landslide area of 43.2 km^2. The total volume of landslides triggered by the Luding earthquake is estimated to be 1.27 km^3, calculated by the power–law relationship between the landslide area and volume [31]. Overall, coseismic landslides were predominantly situated on both sides of the seismogenic fault, with a greater density observed on the west side (SWW plate) in comparison to the east side (NEE plate). Specifically, over 60% of the landslides occurred on the SWW plate, while the remaining 40% were on the NEE plate (Figure 5). More than 70% of landslides develop in areas with a PGA greater than 0.5g, about 20% of coseismic landslides occur in an area with a PGA of 0.4 g, and only a few landslides develop in areas with a PGA less than 0.4 g, which are mainly concentrated in the south of the Xinmin area. Overall, compared to the NEE plate, the development of landslides on the SWW plate is more severe, being significantly larger in scale and greater in number.
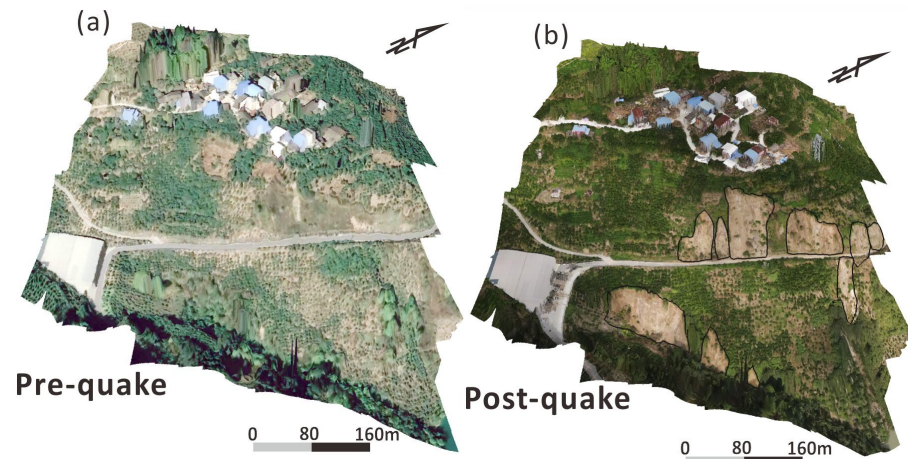
Figure 4. (**a**) Pre-quake image from Google Earth. (**b**) Post-quake image taken by an unmanned aerial vehicle (UAV). The location is 29.418°N, 102.228°E.
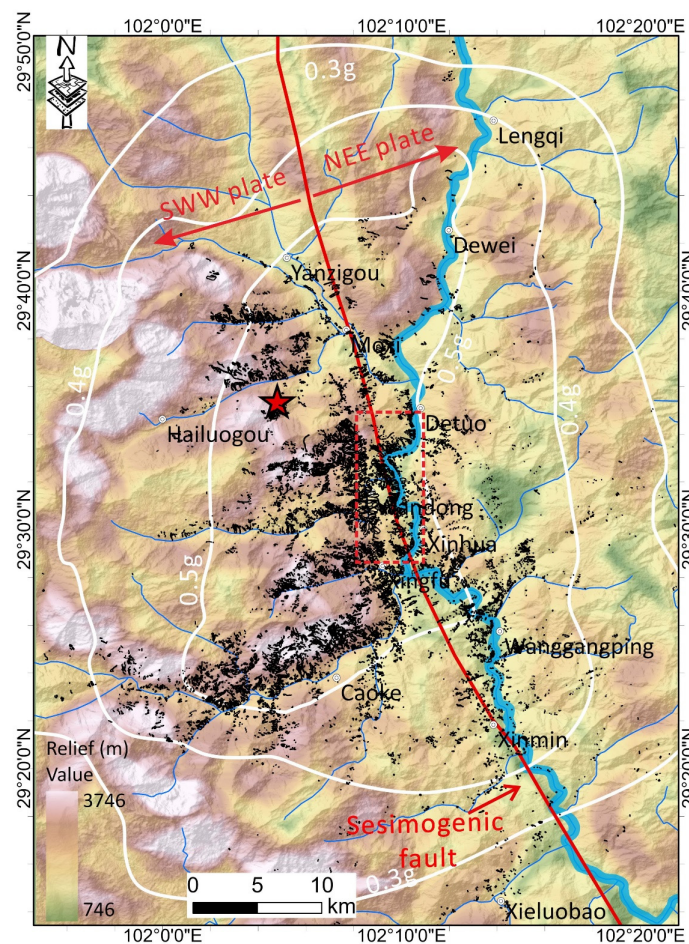

Figure 5. Map showing the distribution of coseismic landslides triggered by the Luding event. The black polygon is the boundary of the landslide, the red star represents the location of the epicenter, and the white line is the PGA distribution. The red dashed box represents the position of Figure 3.

3.2. Related Controlling Factors

Earthquake-induced landslides result from the complex interplay of various controlling factors. The spatial distribution of landslides is influenced not only by seismic factors but also by topographic conditions, geological characteristics, and structural features [32,33]. Currently, there is no unified standard for selecting controlling factors for

earthquake-induced landslides [5]. Based on the previous studies [27,34], we selected elevation, slope angle, aspect, topographic relief, peak ground acceleration (PGA), distance to rivers (dis2rivers), distance to seismogenic fault (dis2fault), and lithology as the ten controlling factors for LR modeling. Elevation and slope features were derived using the ALOS PALSAR Digital Elevation Model (DEM) with 12.5 m resolution. The river networks, including main rivers and major tributaries, were extracted by the elevation data. Meanwhile, we estimated topographic relief within a 2.5 km radius by the elevation data [35] (Figure 5). For peak ground acceleration (PGA) distribution, we collected seismic station records within a 100 km radius of the Luding earthquake, which were obtained from the Sichuan Earthquake Administration. The PGA values were derived based on these seismic station records [27]. Subsequently, we employed the Kriging interpolation method to determine the distribution of the PGA (Figure 5).

3.3. Logistic Regression (LR) Model

Currently, most landslide susceptibility assessment models use various classification methods, including weight of evidence (WOE), forest trees, LR model, SVM, and neural networks [5]. Among these, the LR model is widely used for assessing earthquake-induced landslide hazards due to its simplicity, high efficiency, and accuracy in predictions [5,36]. The fundamental idea of the LR model is to estimate the probabilities of different classes in a binary or multi-class problem through a linear combination of one or more independent variables [37,38]. To map the linear combination to a probability value between 0 and 1, logistic regression employs a special function called the logistic function or sigmoid function. The formula for the LR model is as follows:

$$Z = a + \sum_j b_j x_j \ \mathrm{j} = 1, 2, \ldots \mathrm{m} \tag{1}$$

$$f(z) = \frac{1}{1 + e^{-(z)}} \tag{2}$$

where $f(z)$ represents the probability of landslide occurrence. As z approaches positive infinity, $f(z)$ tends towards 1, and as z approaches negative infinity, $f(z)$ tends towards 0. a is a constant; j denotes the number of independent variables; b_j (j = 1, 2, 3, ..., n) represents the regression coefficients of the model; and x_j (j = 1, 2, 3, ..., n) denotes the independent variables.

The objective of this study is to create a probability estimator for forecasting the areal extent of landslides. In essence, we establish a correlation between the resultant probability and the spatial coverage (e.g., areas marked with a 5% probability of landsliding encompass approximately 5% of the total landslide area) [38,39]. The selection of samples for the model also needs to ensure that the ratio of landslide samples to non-landslide samples aligns with the actual ratio of landslide area to non-landslide area in the study area. We conducted random sampling across the study area at a density of 200 points per square kilometer. Any samples falling within landslide zones were categorized as landslide samples, while those outside these zones served as non-landslide samples. Although this sampling method results in different quantities of landslide and non-landslide samples, this imbalance reflects the true imbalance of landslides occurring within the study area. Consequently, the obtained susceptibility index can accurately represent the probability of landslide occurrences [36,39].

3.4. Modeling Evaluation Index

In this study, we utilized AUC (Area under the Curve) to quantitatively evaluate the importance of various controlling factors and the assessment results of different susceptibility modeling. The AUC, commonly used to assess binary classification model performance [40,41], quantifies the area under the ROC curve. This curve plots the true positive rate against the false positive rate across different threshold settings. A higher AUC

signifies superior model discrimination, with an AUC of 1 indicating a perfect classifier and an AUC of 0.5 suggesting a stochastic model [42].

Otherwise, we used the Jackknife method and single-variable method to further examine the relative importance of the controlling factor following the techniques of [43,44]. The Jackknife method systematically excludes one controlling factor from the dataset each time, recalculates the accuracy of the prediction model, and then analyzes the variability of the estimated values obtained [45,46]. In the Jackknife approach, we iteratively removed a single controlling factor during model training and compared individual model results to assess the influence of removing each controlling factor from the model. If there is a significant decrease in the AUC of the model, it indicates that the deleted controlling factors have a high impact on the accuracy of the model, which means that the model has a strong impact on the spatial distribution of landslides [43,45]. Meanwhile, the single-variable method entails the LR model iteratively on each controlling factor separately to determine their individual importance. A higher model AUC in these instances indicates a stronger independent explanatory power of the feature [44,47].

From the spatial distribution of coseismic landslides, noticeable disparities exist between the SWW and NEE plates, with landslide development being more pronounced in the SWW plate compared to the NEE plate (Figure 5). Additionally, our preliminary findings indicate that landslides on the SWW plate tend to occur in areas characterized by higher elevations and relief features compared to the NEE plate [20,27,34]. Therefore, in this study, we evaluated the potential differences in the influence of various controlling factors on landslide occurrence on both sides by comparing the modeling results of the SWW and NEE plates, as well as all the study area. Subsequently, we established the LR modeling based on different landslide datasets. Otherwise, given the geological heterogeneity on either side of the seismogenic fault, we examined the impact of geological types versus not considering geological types on the LR models during the modeling process. Ultimately, we constructed four LR models and conducted modeling analyses. Considering the randomness of sampling in the modeling process, the models converged prior to a maximum of 50 iterations. Figure 6 presents a flowchart describing this study.
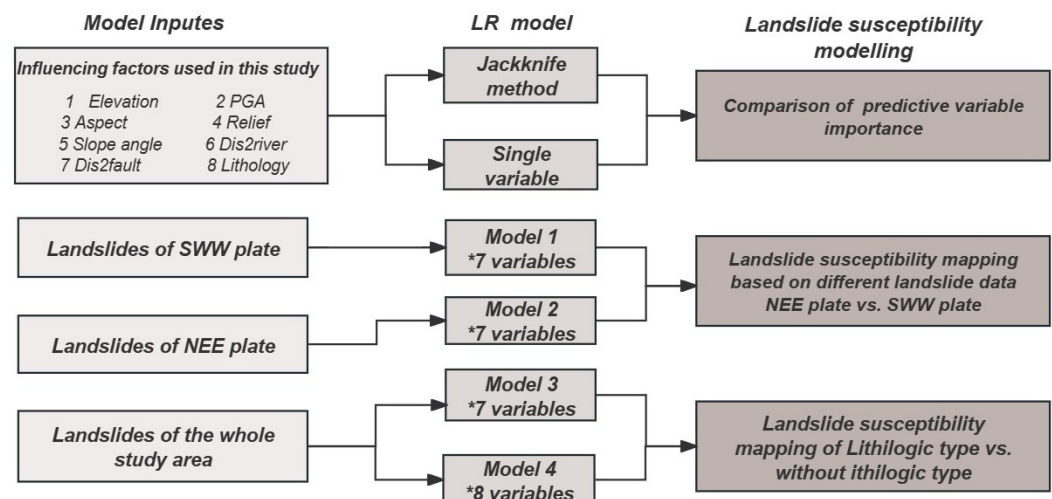

Figure 6. The flowchart of the importance of the controlling factors and landslide susceptibility features in this study. * represents the variables used in LR modeling.

4. Results

4.1. The Importance of Potential Controlling Factors

We computed the AUC values based on the single-variable method to assess the impact of individual controlling factors on landslide occurrences (Figure 7). The results show that, for the entire study area, the elevation, PGA, and dis2fault exhibit the highest AUC values among the continuous variables, all surpassing 0.8, suggesting these factors

have a significant influence on landslide occurrences. Conversely, the slope, relief, and dis2rivers demonstrate relatively low AUC values, mostly below 0.7, with relief having the lowest AUC value at 0.5. Moreover, the predictive outcomes for the two plates (SWW and NEE plates) suggest that different continuous variables may have varying degrees of influence on landslide occurrences. For instance, the AUC results for the PGA and dis2fault in the NEE plate are slightly higher than those in the SWW plate, indicating that these factors might exert a more pronounced control over landslide occurrences in the NEE plate. For the categorical variables, the AUC value of the lithological types for the NEE plate is lower than that of the SWW plate, suggesting that lithology may not contain more explanatory information for the NEE plate. Additionally, the AUC values for aspect remain around 0.6, indicating that different aspects have minor effects on landslide development.
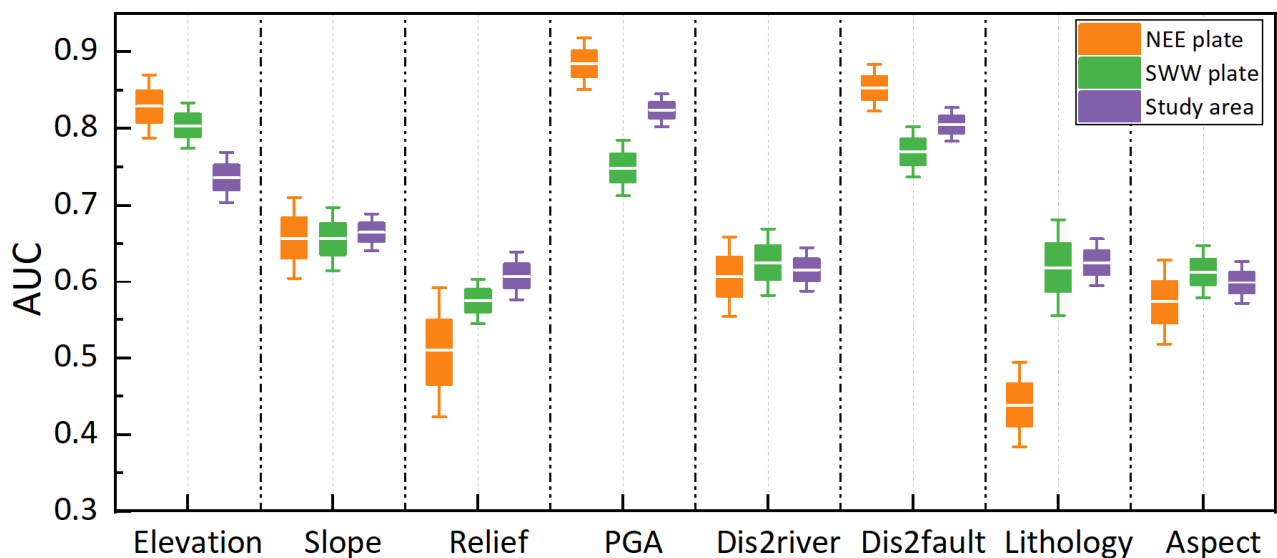

Figure 7. The AUC results for various controlling factors of LR modeling obtained by the single-variable method. The boxplot for each model illustrates the outcomes of a random 50-fold cross-validation.

Figure 8 presents the AUC values of different controlling factors obtained by the Jackknife method. Overall, upon excluding the PGA and dis2fault factors, the AUC values of the model significantly decrease, whereas the removal of dis2rivers and aspect does not result in a noticeable decline in AUC values. This indicates that, from the perspective of the entire study area, the PGA and dis2fault are the primary controlling factors for landslide occurrence, while dis2rivers and aspect have a minor impact on the occurrence of seismic landslides. Additionally, for the NEE plate, the model's AUC value notably decreases after removing the PGA, whereas this trend is not observed for the SWW plate, suggesting that seismic factors exert a greater influence on landslides in the SWW plate compared to the NEE plate. Furthermore, for lithological types, compared to the NEE plate, the model's AUC value significantly decreases when the lithological factor is excluded for the SWW plate, indicating a more pronounced control of lithology on landslide occurrence in the SWW plate. Otherwise, elevation and relief exhibit a similar trend like the lithological factor, which suggests that, besides the PGA, lithology and topographic features are also important environmental variables affecting landslide occurrence in the SWW plate.
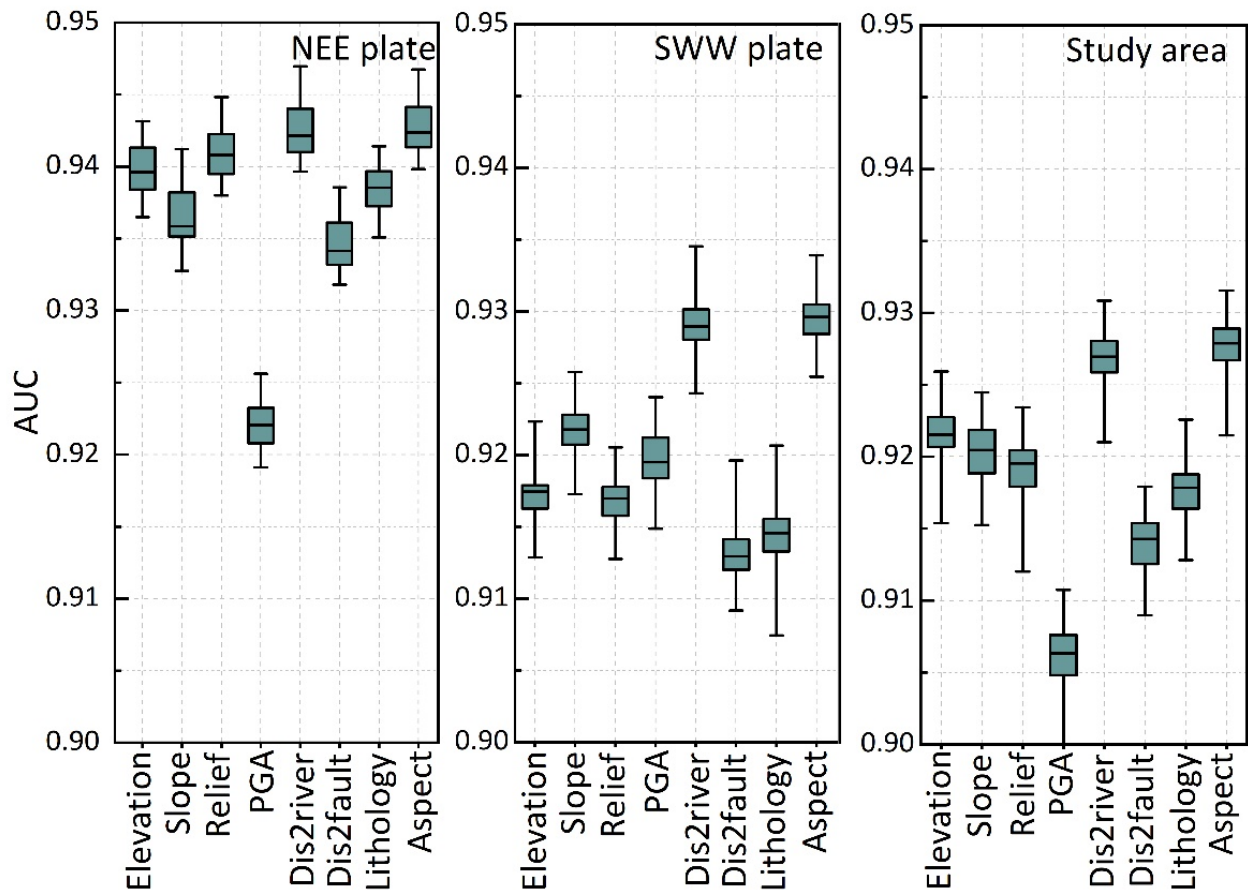
Figure 8. The AUC results for various controlling factors of LR modeling obtained by the Jackknife method. The boxplot for each model illustrates the outcomes of a random 50-fold cross-validation.

Because the model features were standardized using the standard scalar method, the model coefficients can be compared for different controlling factors to estimate the feature importance. For continuous variables, a positive regression coefficient indicates a positive correlation, meaning that, as the independent variable increases, the likelihood of landslide occurrence also increases. By analyzing the regression coefficients, we can interpret the relationship between each continuous variable and landslide occurrence. Figure 9 illustrates the regression coefficients for different controlling factors of coseismic landslides calculated by LR models. The results indicate that, for the SWW plate, NEE plate, or entire study area, elevation, dis2fault, and dist2rivers exhibit negative correlations, while slope, relief, and PGA demonstrate positive correlations. This suggests that landslides are more likely to occur in areas of low elevation and high ground motion. Among these, elevation, PGA, and dis2fault possess the largest absolute regression coefficients, indicating that, compared to the other controlling factors, these three factors have a significant effect on landslide occurrences. Overall, the importance ranking of these controlling factors on coseismic landslides is PGA > elevation > dis2fault > slope > dis2rivers > relief.
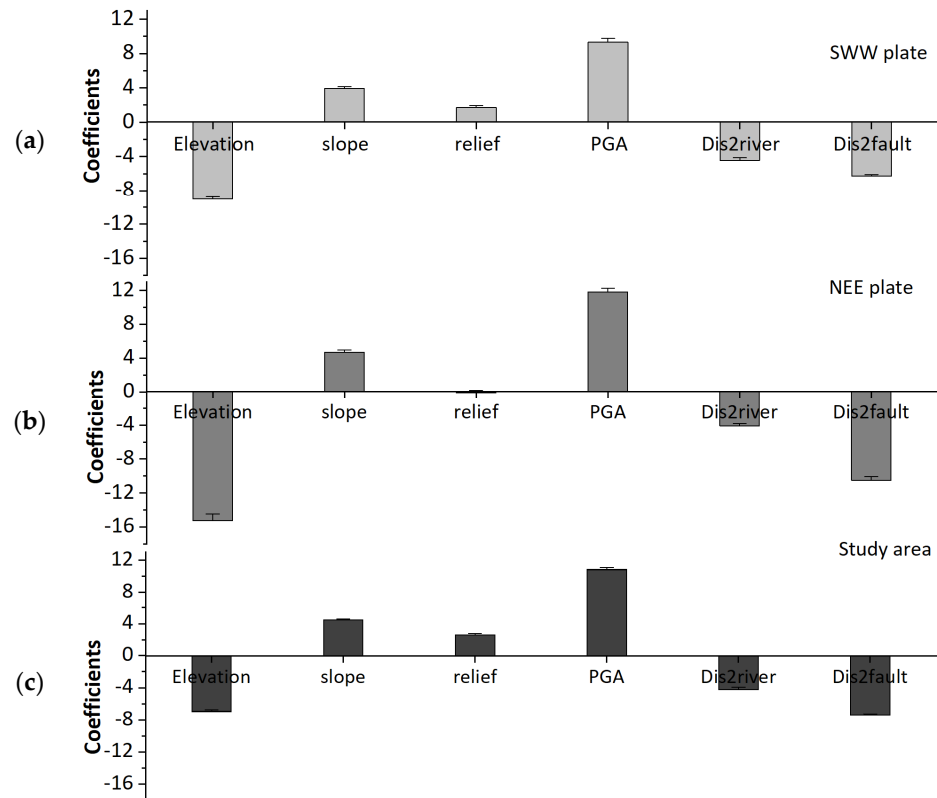
Figure 9. Regression coefficients for different controlling factors of coseismic landslides calculated by LR models: (**a**) SWW plate, located on the west side of the seismogenic fault; (**b**) NEE plate, which is the east side of the seismogenic fault. (**c**) The entire study area.

4.2. Landslide Susceptibility Modeling

Based on the aforementioned study, we constructed the LR models for both the SWW and NEE plates, respectively, and generated landslide probability maps for the study area using these two models (Model 1 and Model 2) (Figure 10). Model 1 is trained by landslide data derived from the NEE plate, whereas Model 2 utilizes landslide data sourced from the SWW plate. The result shows that the high-susceptibility areas predicted by both models are distributed along both sides of the seismogenic faults and the Dadu Rivers, which closely align with the actual landslide distributions (Figure 10). However, it should be noted that the predicted area of moderate- to high-susceptibility zones derived from Model 2 is notably larger than that from Model 1. In local areas, there are also discrepancies in the predictions of both models in localized areas. For instance, in the vicinity of the epicenter, Model 2 shows a significantly higher range of moderate- to high-susceptibility zones compared to Model 1. Moreover, in the Wangdong and Xingfu regions where landslides are most densely concentrated, the predicted occurrence probability from Model 1 is noticeably lower than that from Model 2. Additionally, in the northern region of Caoke and near the Xieluobao area, the predicted result of the moderate- to high-susceptibility area by Model 2 is also greater than that by Model 1. To further compare the results of the predicted probability distributions, we conducted a statistical analysis on the probability values of the two models (Model 1 and 2) (Figure 11). The results indicate that the probability distributions of the two models exhibit a similar trend, characterized by an initial increase followed by a decrease (Figure 11). Specifically, the probability values of Model 1 are mainly concentrated between 0.00005 and 0.002, while those of Model 2 are primarily distributed between 0.004 and 0.02. Compared to Model 1, the probability predictions of Model 2 are roughly higher.
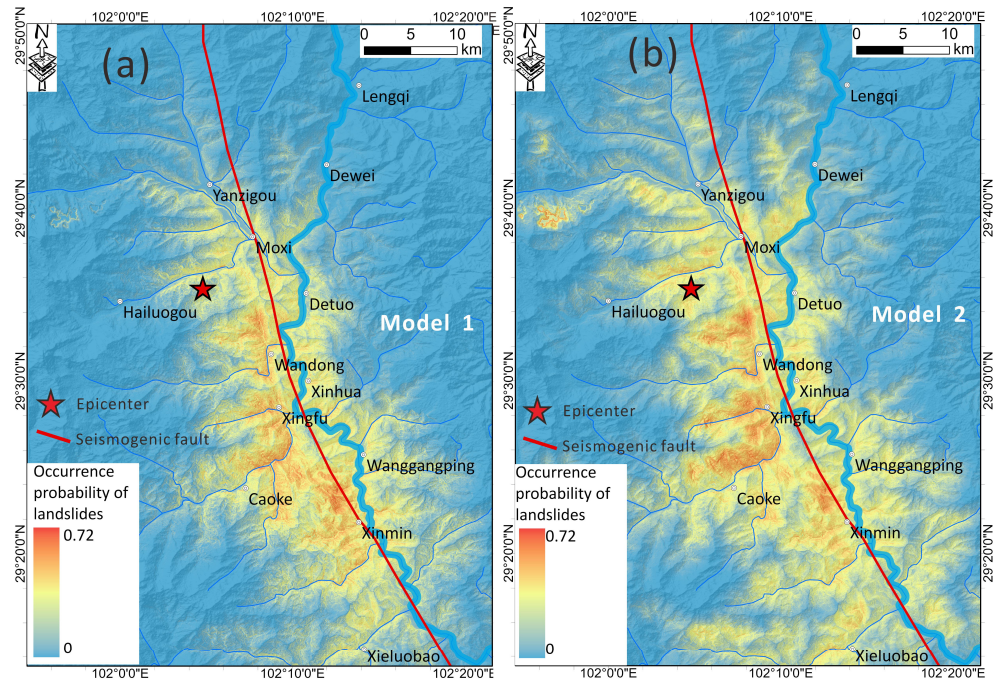
Figure 10. Map showing the predicted results of the occurrence probability of landslides based on two different models. (**a**) The LR model trained by the landslides data of the NEE plate (Model 1). (**b**) The LR model trained by the landslides data of the SWW plate (Model 2).
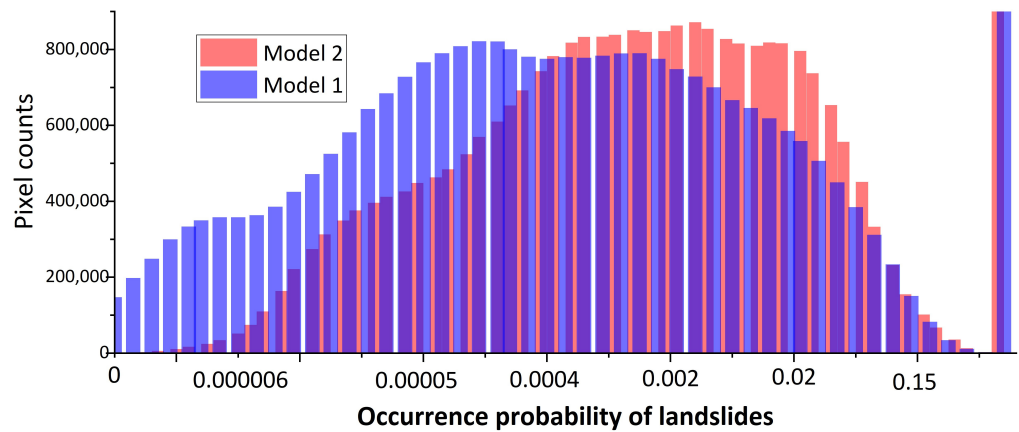

Figure 11. Map showing the probability distribution of landslide occurrence for two evaluation models.

Figure 12 depicts the boxplots of the landslide prediction area and AUC for Model 1 and Model 2. From the boxplots, it is evident that the predicted landslide area by Model 2 of 46.92 km^2 is significantly larger than that by Model 1 of 34.73 km^2. However, the actual landslide area in the study area is 44.29 km^2, indicating that the predicted area by Model 2 is closer to the actual situation. Additionally, we observe that the AUC values of Model 1 are higher than those of Model 2 on the training set, with average AUC values of 0.93 and 0.89, respectively. However, for the validation set, the opposite trend is observed, with Model 2 exhibiting slightly higher AUC values than Model 1.
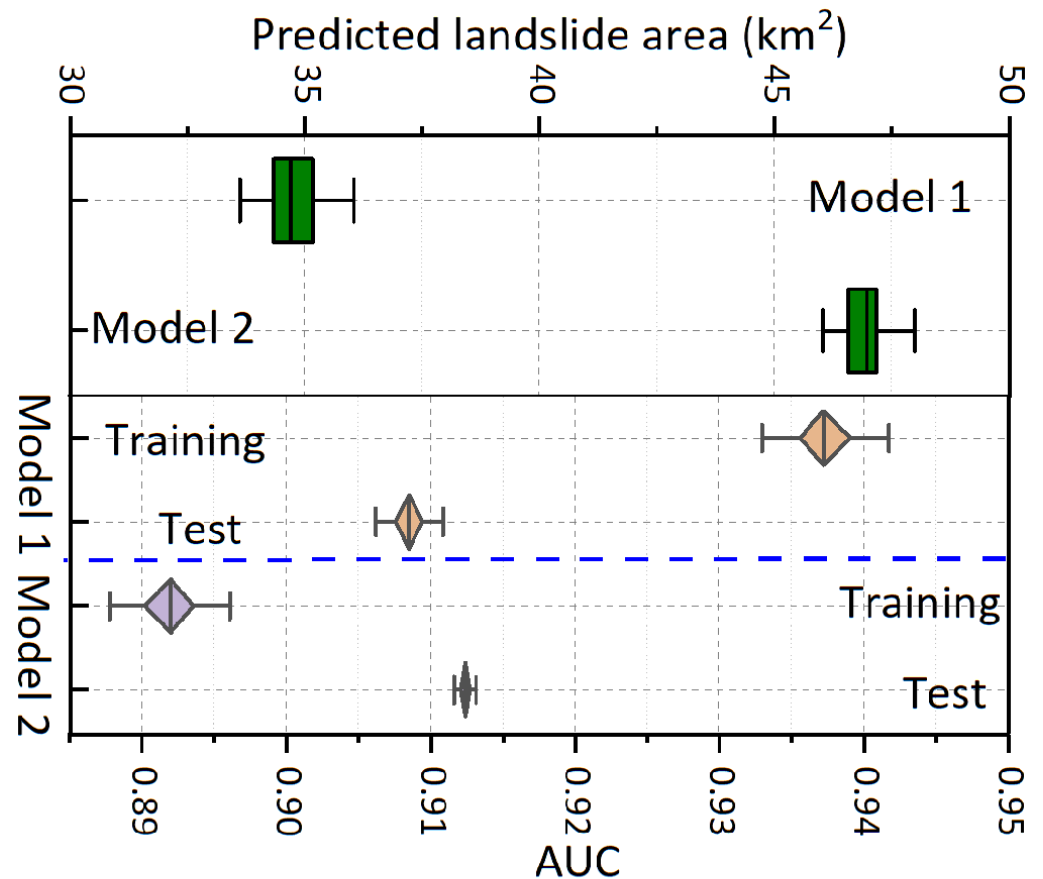
Figure 12. Map showing the predicted landslide area and AUC values based on different models.

In addition, due to the differences in lithological types on both sides of the seismogenic fault, we constructed two LR models, one considering lithology and the other not considering lithology, to compare the influence of lithological types on the assessment results. Figure 13 shows the predicted results of the occurrence probability of landslides based on Models 3 and Model 4, respectively. It can be observed that the predicted results of the two models are roughly consistent in the predicted high-susceptibility areas, mainly concentrated in the Wangdong, Xingfu, and Caoke regions. However, differences exist in the predicted results of the two models in local areas. For instance, in the eastern part of the Caoke area, Model 3 yields notably higher predictions compared to Model 4. This phenomenon could be linked to the prevalence of Triassic limestone and Triassic and Devonian quartz sandstone ($T_L \& D_s$) in the area, the lithological type associated with relatively low landslide incidence. Therefore, due to the spatial differences in lithology, although the overall distribution of the prediction results is consistent, there are still differences at the local scale.

To quantitatively assess the correlation between the occurrence probabilities of landslides predicted by four different models, we randomly selected 10,000 points within the study area and analyzed the correlations between the occurrence probability values of different models. Figure 14a presents a scatter plot of the occurrence probability values of Model 1 and Model 2. The results indicate a linear relationship between the two models, where Model2 = 1.013 * Model1. It should be noted that the slope of the fitted function is 1.013; this is mainly due to the differences in the training landslide datasets used for the two LR models, resulting in slightly higher predictions in Model 2 compared to Model 1. Figure 14b shows scatter plots of the predicted results for Model 3 and Model 4 and indicates a linear relationship between the two models. The slope of the fitted function is 0.994, suggesting that the prediction results of the two models are roughly consistent. In local areas, there are differences in the predictive results between the two models. Overall, the

predictive results of the model considering lithology are higher in local areas compared to those of the model not considering lithology.
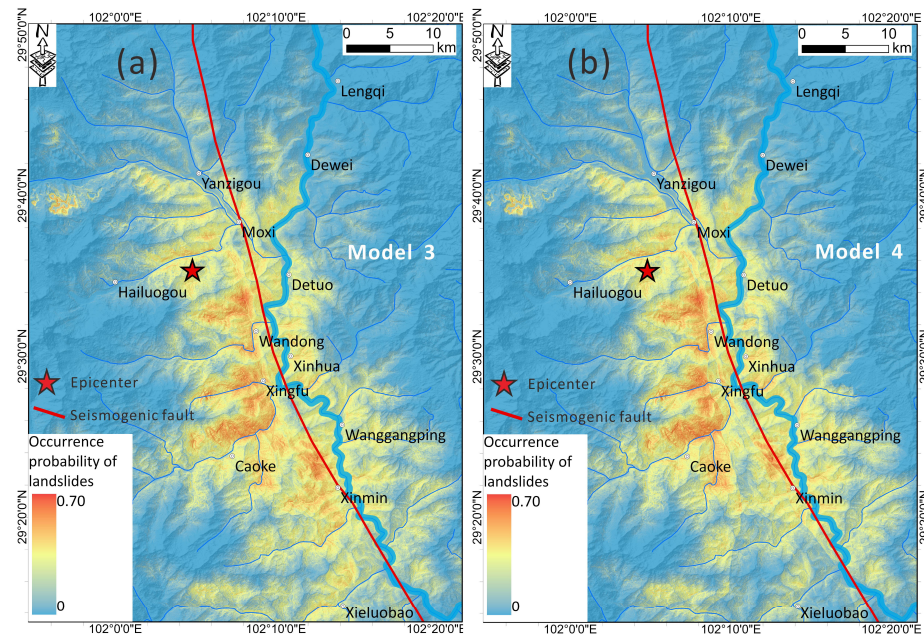

Figure 13. Map showing the predicted results of the occurrence probability of landslides based on two different models. (**a**) The LR model without considering geological types (Model 3). (**b**) The LR model considering geological types (Model 4).
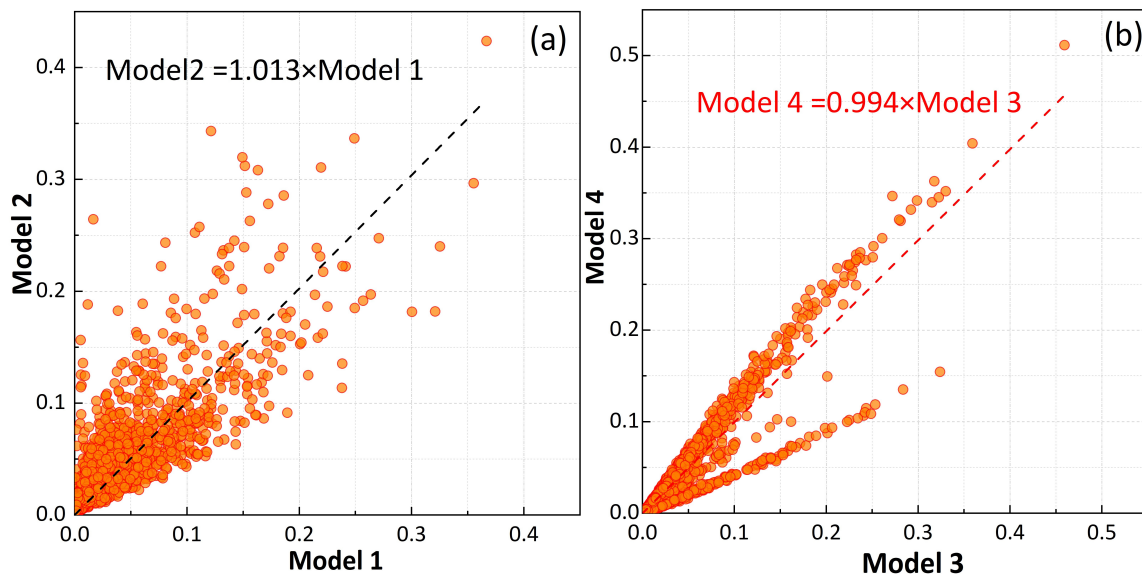

Figure 14. Map showing the correlation between the occurrence probability of landslides for different models. (**a**) The relationship of the predicted results between Model 1 and Model 2. (**b**) The relationship of the predicted results between Model 3 and Model 4.

5. Discussion

Currently, related studies have analyzed the relationship between different influencing factors and the distribution characteristics of landslides for the Luding earthquake event from a statistical perspective [20,21,48]. However, these studies cannot quantitatively analyze the order of importance of different influencing factors. Furthermore, the existing study indicates that, compared to the NEE plate, landslides on the SWW plate are more likely to occur in areas characterized by higher elevations and reliefs, indicating potential

variations in the importance of different influencing factors on the spatial distribution of landslides on both sides of the seismogenic fault [27]. Therefore, we quantitatively assessed the importance of eight causative factors using the Jackknife and univariate methods. The results show that seismic factors have the greatest influence on landslides in the entire study area, followed by elevation, while dis2rivers and topographic relief have little influence on the distribution of landslides. Additionally, the degree of influence of different controlling factors on landslides on both sides of the seismogenic fault varies inconsistently. For example, compared to the NEE plate, the PGA has a greater impact on landslides in the SWW plate. Moreover, excluding lithological factors, the AUC value of the SWW plate significantly decreases for lithological types and aspect, indicating a more pronounced lithological control over landslides in the SWW plate. We attribute this phenomenon primarily to the occurrence of numerous landslides in Permian basalt and tuff in the SWW plate. Therefore, when lithological types are not considered in the SWW plate, the AUC results of the model significantly decrease. Landslides in the NEE plate mainly consist of small-scale shallow landslides, collapses, and rockfalls, so the influence of the PGA on small-scale landslides may be more significant. In contrast, landslides on the SWW plate tend to be larger in scale, and this plate of the seismogenic fault experiences heightened seismic energy along with significant surface deformation [34], indicating a more pronounced control of the seismogenic fault on landslides in the SWW plate.

A detailed and objective inventory of landslides is essential for the regional landslide susceptibility mapping [49,50]. Previous studies have primarily focused on rapid emergency assessments of earthquake-induced landslides following the Luding earthquake, lacking detailed susceptibility mapping of landslides for this event [18,25]. Therefore, based on our updated landslide database [27], we conducted a landslide susceptibility assessment for the Luding event and compared the predicted accuracy of different models. We divided the study area into fishnets of 1 km × 1 km and calculated the predicted landslide area within each fishnet for the above four predicted models. Overall, the high susceptibility zones predicted by different models are distributed along the seismogenic fault and the Dadu Rivers, which is consistent with the actual landslide distribution. However, there are also differences in the predicted results of the two models in local areas. The predicted results based on Model 2 are significantly greater than those based on Model 1, with the predicted landslide areas based on Model 2 being consistent with the actual landslide areas, while the results based on Model 1 are notably lower. The results indicate that Model 1 significantly underestimates the landslide area on the western side of the seismic fault, particularly in the Xingfu and Caoke areas, while overestimating the landslide area in the south of the Xinmin area (Figure 15a,b). The primary reason for this phenomenon is that over 60% of landslides in the entire study area are concentrated in the SWW plate; thus, the predictive model based on landslide data from the SWW plate better reflects the actual landslide distribution. Furthermore, from the AUC results, although Model 1 has a higher AUC value than Model 2 for the training set, the predictive ability of Model 1 significantly decreases compared to Model 2 for the validation set. This result may suggest that Model 1 is overfitting to the training data, leading to a decrease in predictive performance on the validation data, whereas Model 2 demonstrates a more stable performance on the testing data. Otherwise, the predicted landslide areas by Model 3 and Model 4 are roughly consistent with the actual landslide distribution, but there are differences in local areas, such as in the eastern part of the Caoke area (Figure 15c,d). This phenomenon could be linked to the prevalence of Triassic limestone and Triassic and Devonian quartz sandstone ($T_L\&D_s$), as mentioned in the Section 4. Due to the influence of tectonic activity, granite and basalt units exhibit well-developed joints, making this lithological unit more susceptible to landslides under seismic motion [27]. In contrast, quartz sandstone has a higher rock mass strength, making this unit less prone to landslides.
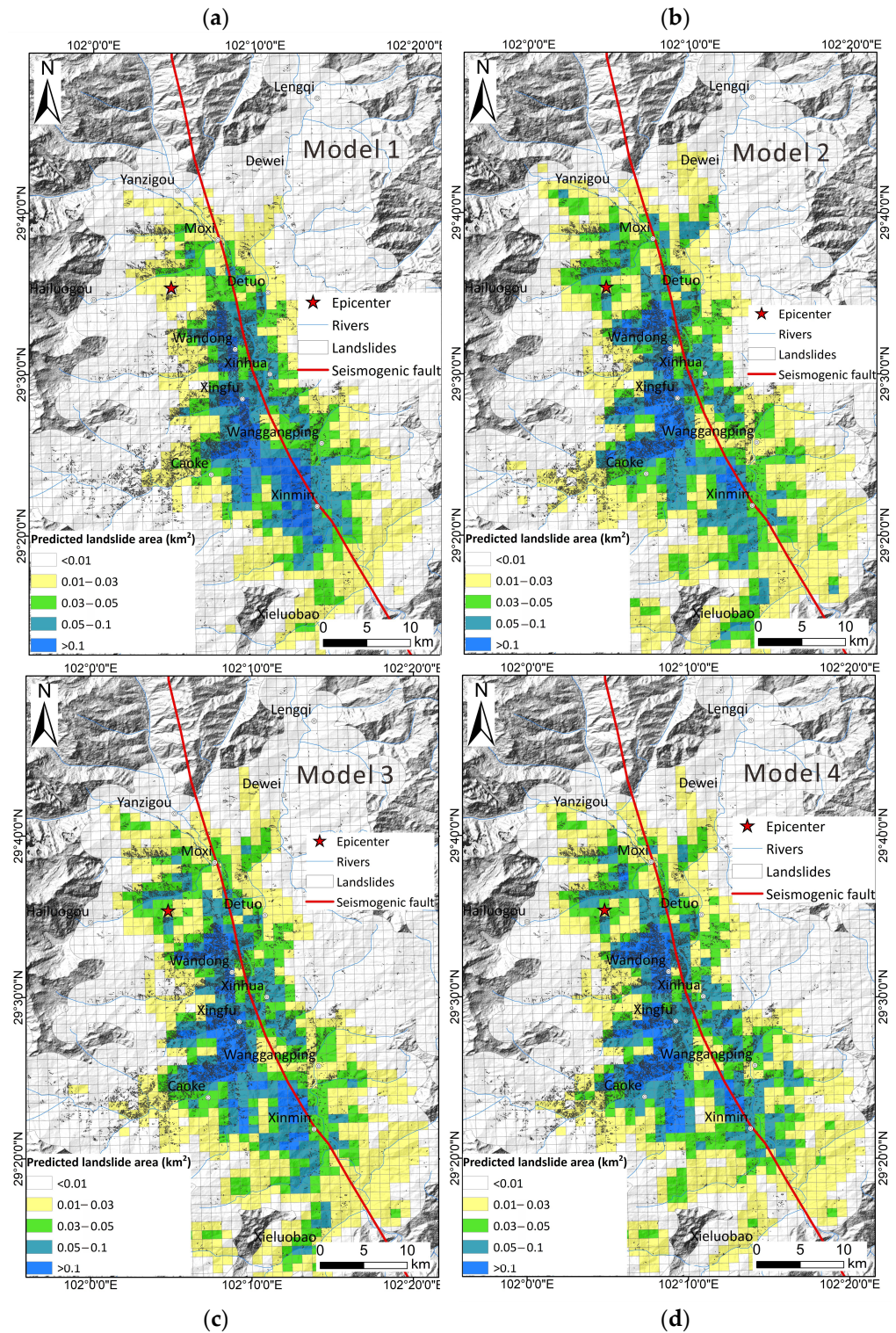
Figure 15. Map showing the predicted landslide area based on different models and actual landslides distribution. (**a**) Model 1; (**b**) Model 2; (**c**) Model 3; (**d**) Model 4. The size of each fishnet is 1 km × 1 km.

6. Conclusions

This paper aims at quantitatively evaluating the importance of different controlling factors and conducting the landslide susceptibility mapping associated with the 2022 Luding earthquake. The results show that, for the entire study area, elevation, PGA, and dis2fault exhibit the highest AUC values among the continuous variables. Overall, the

importance ranking of these controlling factors on coseismic landslides is PGA > elevation > dis2fault > slope > dis2rivers > relief. However, for landslides on both sides of the earthquake fault, different controlling factors may exert varying influences on landslide occurrence. For the NEE plate, the PGA exerts a greater influence on landslides in the SWW plate compared to the NEE plate. The AUC value of the SWW plate significantly decreases for lithological types and aspect, indicating a more pronounced lithological control over landslides in the SWW plate. Otherwise, the susceptibility results based on four models indicate that high-susceptibility areas predicted by different models are distributed along both sides of the seismogenic faults and the Dadu Rivers, which closely align with the actual landslide distribution. In local areas, Model 2 shows a significantly higher range of moderate- to high-susceptibility zones compared to Model 1. The primary reason for this phenomenon is that over 60% of landslides in the entire study area are concentrated in the SWW plate; thus, the predictive model based on landslide data from the SWW plate better reflects the actual landslide distribution. Otherwise, due to the spatial differences in lithology, although the overall distribution of the prediction results of Models 3 and 4 is consistent, there are still differences at the local scale. This phenomenon could be linked to the varied landslide abundance developed in different lithological types.

References

1. Fan, X.; Wang, X.; Dai, L.; Fang, C.; Deng, Y.; Zou, C.; Tang, M.; Wei, Z.; Dou, X.; Zhang, J.; et al. Characteristics and spatial distribution pattern of Ms 6.8 Luding earthquake occurred on September 5, 2022. *J. Eng. Geol.* **2022**, *30*, 1504–1516. [CrossRef]
2. Ma, S.; Lu, Y.; Xia, C.; Liu, X.; Qi, W.; Yuan, R. Brief report of landslides triggered by the 2022 Ms 6.8 Luding earthquake, Sichuan, China. *Landslides* **2023**, *20*, 2695–2707. [CrossRef]
3. Amato, G.; Fiorucci, M.; Martino, S.; Lombardo, L.; Palombi, L. Earthquake-triggered landslide susceptibility in Italy by means of Artificial Neural Network. *Bull. Eng. Geol. Environ.* **2023**, *82*, 160. [CrossRef]
4. Shao, X.; Xu, C. Earthquake-induced landslides susceptibility assessment: A review of the state-of-the-art. *Nat. Hazards Res.* **2022**, *2*, 172–182. [CrossRef]
5. Reichenbach, P.; Rossi, M.; Malamud, B.D.; Mihir, M.; Guzzetti, F. A review of statistically-based landslide susceptibility models. *Earth-Sci. Rev.* **2018**, *180*, 60–91. [CrossRef]
6. Jibson, R.W.; Harp, E.L.; Michael, J.A. A method for producing digital probabilistic seismic landslide hazard maps: An example from the Los Angeles, California, area. *Eng. Geol.* **2000**, *58*, 271–289. [CrossRef]
7. Rodríguez-Peces, M.J.; Pérez-García, J.L.; García-Mayordomo, J.; Azañón, J.M.; Insua-Arévalo, J.M.; Delgado-García, J. Applicability of Newmark method at regional, sub-regional and site scales: Seismically induced Bullas and La Paca rock-slide cases (Murcia, SE Spain). *Nat. Hazards* **2011**, *59*, 1109–1124. [CrossRef]
8. Jibson, R.W. Methods for assessing the stability of slopes during earthquakes—A retrospective. *Eng. Geol.* **2011**, *122*, 43–50. [CrossRef]
9. Lee, C.T. Statistical seismic landslide hazard analysis: An example from Taiwan. *Eng. Geol.* **2014**, *182*, 201–212. [CrossRef]
10. Kavzoglu, T.; Sahin, E.K.; Colkesen, I. Landslide susceptibility mapping using GIS-based multi-criteria decision analysis, support vector machines, and logistic regression. *Landslides* **2014**, *11*, 425–439. [CrossRef]
11. Meena, S.R.; Ghorbanzadeh, O.; Blaschke, T. A comparative study of statistics-based landslide susceptibility models: A case study of the region affected by the gorkha earthquake in nepal. *ISPRS Int. J. Geo-Inf.* **2019**, *8*, 94. [CrossRef]

12. Ma, S.; Shao, X.; Xu, C. Estimating the Quality of the Most Popular Machine Learning Algorithms for Landslide Susceptibility Mapping in 2018 Mw 7.5 Palu Earthquake. *Remote Sens.* **2023**, *15*, 4733. [CrossRef]
13. Merghadi, A.; Yunus, A.P.; Dou, J.; Whiteley, J.; ThaiPham, B.; Bui, D.T.; Avtar, R.; Abderrahmane, B. Machine learning methods for landslide susceptibility studies: A comparative overview of algorithm performance. *Earth-Sci. Rev.* **2020**, *207*, 103225. [CrossRef]
14. Marjanović, M.; Kovačević, M.; Bajat, B.; Voženílek, V. Landslide susceptibility assessment using SVM machine learning algorithm. *Eng. Geol.* **2011**, *123*, 225–234. [CrossRef]
15. Parker, R.N.; Rosser, N.J.; Hales, T.C. Spatial prediction of earthquake-induced landslide probability. *Nat. Hazards Earth Syst. Sci. Discuss.* **2017**, *2017*, 1–29. [CrossRef]
16. Yang, Z.; Xu, C.; Shao, X.; Ma, S.; Li, L. Landslide susceptibility mapping based on CNN-3D algorithm with attention module embedded. *Bull. Eng. Geol. Environ.* **2022**, *81*, 412. [CrossRef]
17. Wu, L.; Liu, R.; Ju, N.; Zhang, A.; Gou, J.; He, G.; Lei, Y. Landslide mapping based on a hybrid CNN-transformer network and deep transfer learning using remote sensing images with topographic and spectral features. *Int. J. Appl. Earth Obs. Geoinf.* **2024**, *126*, 103612. [CrossRef]
18. Wang, X.; Fang, C.; Tang, X.; Dai, L.; Fan, X.; Xu, Q. Research on emergency evaluation of landslides induced by Luding Ms6.8 Earthquake. *Geomat. Inf. Sci. Wuhan Univ.* **2022**, *48*, 25–35. [CrossRef]
19. Huang, Y.; Xie, C.; Li, T.; Xu, C.; He, X.; Shao, X.; Xu, X.; Zhan, T.; Chen, Z. An open-accessed inventory of landslides triggered by the Ms 6.8 Luding earthquake, China on 5 September 2022. *Earthq. Res. Adv.* **2023**, *3*, 100181. [CrossRef]
20. Zhao, B.; Hu, K.; Yang, Z.; Liu, Q.; Zou, Q.; Chen, H.; Zhang, W.; Zhu, L.; Su, L.-J. Geomorphic and tectonic controls of landslides induced by the 2022 Luding earthquake. *J. Mt. Sci.* **2022**, *19*, 3323–3345. [CrossRef]
21. Dai, L.; Fan, X.; Wang, X.; Fang, C.; Zou, C.; Tang, X.; Wei, Z.; Xia, M.; Wang, D.; Xu, Q. Coseismic landslides triggered by the 2022 Luding Ms6.8 earthquake, China. *Landslides* **2023**, *20*, 1277–1292. [CrossRef]
22. Chen, B.; Li, Z.; Huang, W.; Liu, Z.; Zhang, C.; Du, J.; Song, C.; Ding, M.; Zhu, W.; Zhang, S.; et al. Spatial Distribution and Influencing Factors of Geohazards Induced by the 2022 Mw 6.6 Luding (Sichuan, China) Earthquake. *J. Earth Sci. Environ.* **2022**, *44*, 971–985. [CrossRef]
23. Guo, C.; Li, C.; Yang, Z.; Ni, J.; Zhong, N.; Wang, M.; Yan, Y.; Song, D.; Zhang, Y.; Zhang, X.; et al. Characterization and spatial analysis of coseismic landslides triggered by the Luding Ms 6.8 earthquake in the Xianshuihe fault zone, Southwest China. *J. Mt. Sci.* **2024**, *21*, 160–181. [CrossRef]
24. Djukem, D.L.W.; Fan, X.; Braun, A.; Chevalier, M.-L.; Wang, X.; Dai, L.; Fang, C.; Zhang, X.; Gorum, T.; Xu, Q.; et al. Traditional and modified Newmark displacement methods after the 2022 Ms 6.8 Luding earthquake (Eastern Tibetan Plateau). *Landslides* **2024**, *21*, 807–828. [CrossRef]
25. Liu, J.; Wang, T.; Du, J.; Chen, K.; Huang, J.; Wang, H.; Ruan, Q.; Feng, F. Emergency rapid assessment of landslides induced by the Luding MS6.8 earthquake in Sichuan of China. *Hydrogeol. Eng. Geol.* **2023**, *50*, 84–94. [CrossRef]
26. Ma, S.; Xu, C. Applicability of Two Newmark Models in the Assessment of Coseismic Landslide Hazard and Estimation of Slope-Failure Probability: An Example of the 2008 Wenchuan Mw 7.9 Earthquake Affected Area. *J. Earth Sci.* **2019**, *30*, 1020–1030. [CrossRef]
27. Shao, X.; Ma, S.; Xu, C.; Xie, C.; Li, T.; Huang, Y.; Huang, Y.; Xiao, Z. Landslides triggered by the 2022 Ms. 6.8 Luding strike-slip earthquake: An update. *Eng. Geol.* **2024**, *335*, 107536. [CrossRef]
28. Bai, M.; Chevalier, M.L.; Pan, J.; Replumaz, A.; Leloup, P.H.; Métois, M. Southeastward increase of the late Quaternary slip-rate of the Xianshuihe fault, eastern Tibet. Geodynamic and seismic hazard implications. *Earth Planet. Sci. Lett.* **2018**, *485*, 19–31. [CrossRef]
29. Guo, R.; Li, L.; Zhang, W.; Zhang, Y.; Tang, X.; Dai, K.; Li, Y.; Zhang, L.; Wang, J. Kinematic Slip Evolution During the 2022 Ms 6.8 Luding, China, Earthquake: Compatible with the Preseismic Locked Patch. *Geophys. Res. Lett.* **2023**, *50*, e2023GL103164. [CrossRef]
30. Li, Y.; Zhao, D.; Shan, X.; Gao, Z.; Huang, X.; Gong, W. Coseismic Slip Model of the 2022 Mw 6.7 Luding (Tibet) Earthquake: Pre- and Post-Earthquake Interactions with Surrounding Major Faults. *Geophys. Res. Lett.* **2022**, *49*, e2022GL102043. [CrossRef]
31. Xu, C.; Xu, X.; Shen, L.; Yao, Q.; Tan, X.; Kang, W.; Ma, S.; Wu, X.; Cai, J.; Gao, M.; et al. Optimized volume models of earthquake-triggered landslides. *Sci. Rep.* **2016**, *6*, 29797. [CrossRef] [PubMed]
32. Tanyas, H.; Rossi, M.; Alvioli, M.; van Westen, C.J.; Marchesini, I. A global slope unit-based method for the near real-time prediction of earthquake-induced landslides. *Geomorphology* **2019**, *327*, 126–146. [CrossRef]
33. He, Q.; Wang, M.; Liu, K. Rapidly assessing earthquake-induced landslide susceptibility on a global scale using random forest. *Geomorphology* **2021**, *391*, 107889. [CrossRef]
34. Ma, S.; Shao, X.; Xu, C.; Chen, X.; Lu, Y.; Xia, C.; Qi, W.; Yuan, R. Distribution pattern, geometric characteristics and tectonic significance of landslides triggered by the strike-slip faulting 2022 Ms 6.8 Luding earthquake. *Geomorphology* **2024**, *453*, 109138. [CrossRef]
35. Gorum, T.; van Westen, C.J.; Korup, O.; van der Meijde, M.; Fan, X.; van der Meer, F.D. Complex rupture mechanism and topography control symmetry of mass-wasting pattern, 2010 Haiti earthquake. *Geomorphology* **2013**, *184*, 127–138. [CrossRef]
36. Shao, X.; Ma, S.; Xu, C. Hazard assessment modeling and software development of earthquake-triggered landslides in the Sichuan–Yunnan area, China. *Geosci. Model Dev.* **2023**, *16*, 5113–5129. [CrossRef]

37. Dai, F.C.; Lee, C.F. Landslide characteristics and slope instability modeling using GIS, Lantau Island, Hong Kong. *Geomorphology* **2002**, *42*, 213–228. [CrossRef]

38. Nowicki Jessee, M.A.; Hamburger, M.W.; Allstadt, K.; Wald, D.J.; Robeson, S.M.; Tanyas, H.; Hearne, M.; Thompson, E.M. A global empirical model for near-real-time assessment of seismicallyinduced landslides. *J. Geophys. Res. Earth Surf.* **2019**, *123*, 1835–1859. [CrossRef]

39. Shao, X.; Ma, S.; Xu, C.; Zhou, Q. Effects of sampling intensity and non-slide/slide sample ratio on the occurrence probability of coseismic landslides. *Geomorphology* **2020**, *363*, 107222. [CrossRef]

40. Cantarino, I.; Carrion, M.A.; Goerlich, F.; Martinez Ibañez, V. A ROC analysis-based classification method for landslide suscepti-bility maps. *Landslides* **2018**, *16*, 265–282. [CrossRef]

41. Swets, J.A. Measuring the accuracy of diagnostic systems. *Science* **1988**, *240*, 1285–1293. [CrossRef] [PubMed]

42. Brenning, A. Spatial prediction models for landslide hazards: Review, comparison and evaluation. *Nat. Hazards Earth Syst. Sci.* **2005**, *5*, 853–862. [CrossRef]

43. Bloom, C.K.; Singeisen, C.; Stahl, T.; Howell, A.; Massey, C.; Mason, D. Coastal earthquake-induced landslide susceptibility during the 2016 Mw 7.8 Kaikōura earthquake, New Zealand. *Nat. Hazards Earth Syst. Sci.* **2023**, *23*, 2987–3013. [CrossRef]

44. Lombardo, L.; Fubelli, G.; Amato, G.; Bonasera, M. Presence-only approach to assess landslide triggering-thickness susceptibility: A test for the Mili catchment (north-eastern Sicily, Italy). *Nat. Hazards* **2016**, *84*, 565–588. [CrossRef]

45. Lombardo, L.; Mai, P.M. Presenting logistic regression-based landslide susceptibility results. *Eng. Geol.* **2018**, *244*, 14–24. [CrossRef]

46. Obanion, M.; Olsen, M. Predictive seismically-induced landslide hazard mapping in Oregon using a maximum entropy model (MaxEnt). In Proceedings of the 10th National Conference in Earthquake Engineering, Anchorage, AK, USA, 21–25 July 2014; Earthquake Engineering Research Institute: Anchorage, AK, USA, 2014.

47. Williams, F.; McColl, S.; Fuller, I.; Massey, C.; Smith, H.; Neverman, A. Intersection of fluvial incision and weak geologic structures cause divergence from a universal threshold slope model of landslide occurrence. *Geomorphology* **2021**, *389*, 107795. [CrossRef]

48. Zhang, J.; Yang, Z.; Meng, Q.; Wang, J.; Hu, K.; Ge, Y.; Su, F.; Zhao, B.; Zhang, B.; Jiang, N.; et al. Distribution patterns of landslides triggered by the 2022 Ms 6.8 Luding earthquake, Sichuan, China. *J. Mt. Sci.* **2023**, *20*, 607–623. [CrossRef]

49. Harp, E.; Keefer, D.; Sato, H.; Yagi, H. Landslide inventories: The essential part of seismic landslide hazard analyses. *Eng. Geol.* **2011**, *122*, 9–21. [CrossRef]

50. Guzzetti, F.; Mondini, A.C.; Cardinali, M.; Fiorucci, F.; Santangelo, M.; Chang, K.-T. Landslide inventory maps: New tools for an old problem. *Earth-Sci. Rev.* **2012**, *112*, 42–66. [CrossRef]